Structural defects in 2D MoS2 nanosheets and their roles in the adsorption of airborne elemental mercury

Haitao Zhao, Xueliang Mu, Chenghang Zheng, Shaojun Liu, Yanqiu Zhu, Xiang Gao and Tao Wu

University of Nottingham
UK | CHINA | MALAYSIA

University of Nottingham Ningbo China, 199 Taikang East Road, Ningbo, 315100, China

First published 2018

University of Nottingham
UK | CHINA | MALAYSIA

Structural defects in 2D MoS_2 nanosheets and their roles in the adsorption of airborne elemental mercury

Haitao Zhao [ab], Xueliang Mu [b], Chenghang Zheng [a], Shaojun Liu [a], Yanqiu Zhu [c], Xiang Gao*[a] and Tao Wu*[b]

a. Zhejiang University, Hangzhou 310027, China.
b. Key Laboratory of Clean Energy Conversion Technologies, The University of Nottingham Ningbo China, Ningbo 315100, China.
c. University of Exeter, Exeter EX4 4QF, UK.

**Corresponding author:* tao.wu@nottingham.edu.cn; xgao@zju.edu.cn

ABSTRACT

In this research, ab initio calculations and experimental approach were adopted to reveal the mechanism of Hg^0 adsorption on MoS_2 nanosheets that contain various types of defects. The ab initio calculation showed that, among different structural defects, S vacancies (Vs) in the MoS_2 nanosheets exhibited outstanding potential to strongly adsorb Hg^0. The MoS_2 material was then prepared in a controlled manner under conditions, such as temperature, concentration of precursors, etc., that were determined by adopting the new method developed in this study. Characterisation confirmed that the MoS_2 material is of graphene-like layered structure with abundant structural defects. The integrated dynamic and steady state (IDSS) testing demonstrated that the Vs-rich nanosheets showed excellent Hg^0 adsorption capability. In addition, ab initial calculation on charge density difference, PDOS, and adsorption pathways revealed that the adsorption of Hg^0 on the Vs-rich MoS_2 surface is non-activated chemisorption.

Keywords: MoS_2 nanosheet, structural defect, Hg^0 adsorption, ab initio calculation

1. Introduction

The airborne elemental mercury (Hg^0) is the most dominant and problematic form of mercury[1-3] because it is highly volatile and insoluble in water [4-6]. It can travel in the air over a long-distance, bio-accumulate in the ecosystem and is persistent in the environment [7]. Therefore, it has significant impacts on ecosystem and human being's health. In the past two decades, mercury emission has become a global concern and has

attracted tremendous amount of attention in the development of novel materials for the mercury removal[8].

Technologies for the removal of elemental mercury in gas phase is highly demanded in industries such as coal-fired power plants, petrochemical processes, incineration plants[9-13]. Currently, activated carbon is commercially applied in power plants for elemental mercury removal[14]. However, the spent carbon is still a hazardous material and may compromise fly ash as a saleable by-product[15-17]. Therefore, the development of alternative non-carbon-based sorbents is necessary for mercury emission control in industry[18-20].

Recently, 2-dimensional transition-metal dichalcogenides (2D-TMDs) have attracted increasing attention due to their unique structural features and have been applied in various industrial processes[21]. MoS_2 is a 2D-TMDs material that has layered structure, strong in-plane bonding and weak out-of-plane interactions, which shows excellent electrical, physical, chemical and mechanical properties[22]. To date, MoS_2 has been successfully applied in various applications for reducing the emission of hazardous pollutants[23-26]. However, not much work has been carried out on the application of MoS_2 in the adsorption of elemental mercury (Hg^0).

In our previous studies, a suite of Mo-based transition metal oxides and sulphides were investigated as candidate materials for Hg^0 removal[27, 28]. The presence of Mo species in metal oxides was found to promote Hg^0 removal[27], and the MoS_2 nanosheets exhibited outstanding Hg^0 removal performance [16, 29-31]. The effects of temperature, space velocity, the existence of other gas species and the recovery of Hg0 as a resource (or for permanent disposal) have been studied in detail[30, 31].However, the effect of structural defects of MoS_2 nanosheets on Hg^0 adsorption remains unclear.

Normally, structural defects provide extraordinary opportunities to tailor the intrinsic properties and create new functionalities. For 2D materials, structural defects have been

found to have strong influence on the electron−electron interactions. Different types of defects in MoS_2 nanosheets were found playing important roles in various applications[32]. However, the roles of different types of defects in MoS_2 nanosheets in airborne Hg^0 adsorption remain unexplored.

In this research, ab initio calculation was conducted to study mechanism of the adsorption of Hg^0 on MoS_2 nanosheets with different types of defects. A novel method was developed to determine conditions for the rapid synthesis of MoS_2-containing materials with desired functions. Characterisation of defect-rich MoS_2 containing materials was then carried out, followed by the testing of the performance of this material in Hg^0 adsorption.

2. Materials and methods

2.1 Equipment

A dedicated rig was adopted for the evaluation of mercury adsorption performance of the MoS_2 materials. The rig consists of a mercury analyser, elemental mercury calibrator/generator, dilution probe controller, mercury sample conditioner, which was used to generate elemental mercury and to perform online analysis of elemental and oxidised mercury. A flue gas analyser was used to analyse other gas compounds in the simulated flue gas from coal-fired power stations. The details of this experimental set-up are described elsewhere[27-29, 32].

2.2 Computational method

ab initio calculation was performed using Density Functional Theory – Dispersion Correction (DFT-D) with exchange-correlation functional GGA-PW91-OBS[33]. The ultra soft pseudo potential (USPP)[34] was implemented. It was assumed that there were no atomic layers being constrained in the MoS_2 (4X4)[35]. Furthermore, the transition state (TS) confirmation was implemented following the nudged elastic band (NEB) method.

The p-band center (ΔE_I), following the d-band model approach [36], is adopted to study the formation of chemisorption bonds[37].

$$\Delta E_I \propto \frac{V^2}{|\varepsilon_p - \varepsilon_s|} \quad (1)$$

where the right side term represents the attraction between adsorbate and adsorbent , in which V is the coupling matrix element; $\boldsymbol{\varepsilon_s}$ is the energy level of the most active band in the adsorbate and was set to be the value of Hg^0 s-orbital band center; $\boldsymbol{\varepsilon_p}$ is the energy level of p orbitals, which is the active orbital of atoms and can be calculated by $\boldsymbol{\varepsilon_p} = \frac{\int_{-\infty}^{fermi} x\rho(x)\,dx}{\int_{-\infty}^{fermi} \rho(x)\,dx}$ (the x and $\boldsymbol{\rho(x)}$ correspond to energy (eV) and DOS (electron/eV), respectively, while integral domain is from the minimum energy to fermi-energy of p-orbital electrons).

The adsorption energy ($\boldsymbol{E_{ads}}$) is calculated by,

$$\boldsymbol{E_{ads} = E_{Hg+MoS_2} - (E_{Hg} + E_{MoS_2})} \quad (2)$$

where, $\boldsymbol{E_{Hg}}$ is ground state energy of the free Hg^0 atom in a $(11\ Å)^3$ supercell; $\boldsymbol{E_{MoS_2}}$ is total energy of the $\boldsymbol{(4 \times 4)}$ supercell, and $\boldsymbol{E_{Hg+MoS_2}}$ is optimized total energy of the system with a Hg^0 atom being adsorbed and the $\boldsymbol{(4 \times 4)}$ supercell.

Vacancy energy is calculated by,

$$\boldsymbol{E_V = (E_{DFS} + E_{MA}) - E_{PFS}} \quad (3)$$

where, $\boldsymbol{E_{PFS}}$ is total energy of the defect-free structure; $\boldsymbol{E_{DFS}}$ is total energy of the structure having a particular type of vacancy; while $\boldsymbol{E_{MA}}$ is total energy of missing atoms in the vacancies.

2.3 Sample preparation

The Vs-rich MoS_2 nanosheets containing material was prepared using incipient wetness impregnation (IWI) followed by sulphur-chemical vapour reaction (S-CVR) method[16, 32]. The precursor used was $(NH_4)_6Mo_7O_{24}•4H_2O$, while the commercial mesoporous γ-Al_2O_3 (V-SK Co., Ltd.) was selected as the support. The stable phases of the molybdenum containing materials under different temperatures and partial pressure were predicted using FactSage™ 6.3 with a Phase Diagram module [38], which was then used to guide the selection of appropriate preparation conditions to ensure the formation of MoS_2 nanosheets under a controlled manner. By following the predicted conditions, the γ-Al_2O_3 saturated with $(NH_4)_6Mo_7O_{24}•4H_2O$ solution was dried in an oven at 120 °C for 24 h and calcined in air at 520 °C for 12 h. Prior to S-CVR, the sample was pre-heated to 500°C and kept isothermal for 1 h with nitrogen purge at a flow rate of 100 ml/min to remove moisture and other adsorbed matters. The samples were then in situ sulphided with a H_2S/H_2 gas mixture (10 vol.% H_2) at a flow rate of 20 ml/min under a desired temperature for 3 h. A similar procedure for sample preparation was described in detail elsewhere[16, 32].

2.4 Characterization of the MoS_2 material

X-Ray Photoelectron Spectroscope (XPS) analysis was conducted using a Kratos AXIS Ultra DLD spectrometer with an Al K_α radiation source at room temperature and under a vacuum condition (10^{-7} Pa)[39]. Samples were analyzed using a Raman Renishaw RM2000. The pump radiation was supplied by a diode laser of 514 nm and the Raman emission was focused using a 50 × objective[40]. The crystallinity of the sample was analysed using an X-Ray Diffraction (XRD, Bruker D8 A25, Germany), during which the CuK_α radiation was set as 40 kV and 40 mA, and scanning was carried out from 10˚ to 90˚ [32]. A high-resolution transmission electron microscopy (HRTEM) (JEM 2100) operated at 200 kV was used to study the morphology of the samples[39].

In-situ Diffuse Reflectance Infrared Fourier Transform Spectroscopy (In-situ DRIFTS) was applied to investigate the surface acid sites by using NH_3 as the alkaline probe molecule. The IR spectra were recorded using a Fourier Transform Infrared Spectrometer (Bruker V70, USA) equipped with a Praying Mantis™ reaction chamber (Harrick, USA). Similar experimental procedures are described elsewhere[32]. Adsorption/desorption of NH_3 (as the base probe molecule) on the surface of the sample was studied by using Temperature Programmed Desorption (TPD) following similar procedures as the in-situ DRIFTS experiments.

2.5 Evaluation of mercury adsorption performance

The samples were evaluated by using an integrated Hg^0-TPSR dynamic and steady state (IDSS) method. The Hg^0-TPSR and IDSS were carried out using a dedicated experimental rig that equipped with a mercury generator (Tekran 3310, USA) and mercury analysis system (Tekran 3300RS, USA) as described in our previous research[27].

Based on qualitative analysis, the characteristics of Hg^0 capture were extracted from the profile generated from the Hg^0-TPSR experiment.

Quantitative analysis of the Hg^0-TPSR experimental results was conducted to study the instantaneous Hg^0 removal efficiency, the adsorption and desorption of Hg^0 on the surface of the adsorbents.

The maximum instantaneous Hg^0 removal efficiency (ΔX_{max}) was calculated using Equation (4).

$$\Delta X_{max} = \frac{[Hg^0]_{in} - [Hg^0]_{out}}{[Hg^0]_{in}} \times 100 \quad (4)$$

Area of the adsorption region (S_a) and the desorption region (S_d), which corresponds to the areas below or above the concentration baseline, was determined by the integration of Equation (5).

$$S = \int_{t1}^{t2} f(t)dt \quad (5)$$

where, t_1 is the starting time of adsorption/desorption, min; t_2 is the ending time of adsorption/desorption, min; f(t) is the change of Hg^0 concentration as a function of time; S is the area determined using the integration method, $min \cdot \mu g \cdot m^{-3}$.

Based on the Hg^0-TPSR dynamic transient analysis, a steady-state evaluation of Hg^0 adsorption performance was further conducted. The samples were evaluated under the same temperature (50°C) and Hg^0 concentration (30 $\mu g/m^3$) for at least 180 min after the reactions had reached steady state.

3. Results and discussion

3.1 Computational study

3.1.1 Geometric structure of defective MoS_2 nanosheets

The MoS_2 nanosheets normally contain different structural defects in its crystal lattices, which are the potential sites for airborne Hg^0 capture [41].The MoS_2 nanosheets with defect-free surface as well as those with different types of defects, such as vacancies with the absence of one S atom (V_S), the absence of two S atoms (V_{S2}) and the absence of one Mo atom (V_{Mo}), were investigated in detail in this study.

It is found that the atoms around the S vacancy exhibit different extents of inward relaxation depending on the number of S atoms that are absent. This is because the radius of an S^{2-} ion (0.184nm) is much larger than that of a Mo^{4+} ion (0.065nm) [42, 43] and this type of inward relaxation is commonly seen in defective surface structures with large size atoms being removed from a defect-free surface.

For a Mo vacancy, its neighbouring atoms show an outward relaxation due to the weakened electrostatic attraction force between the NA S atom and the Mo vacancy. Additionally, the outward relaxation of the NA S atom is greater than that of the NA Mo atoms. That means the relative distance between upper S plane and the second NA Mo atoms becomes greater as compared with no relaxation occurred. Based on the

calculation, after relaxation, the distance between the NA S atoms and the Mo vacancy increased by 2.61%, while the distance between the NA Mo atoms and the Mo vacancy was shorten by 0.63% (as shown in Table 1). It can be concluded that absence of Mo atom(s) leads to the formation of Mo vacancies that are negative charged, which have the potential to facilitate the adsorption of metals in oxidized state. Therefore, the oxidation of Hg species (for example, HgCl, HgO) could have affinity with such kind of positions.

However, driven by the weakened electrostatic repulsion between the nearest adjacent (NA) S atoms and the S vacancy, the extent of the inward relaxation of the NA S atom is greater than that of the NA Mo atoms. Therefore, the distances between V_S and the NA Mo atoms and between V_S and the NA S atoms are shortened by 0.04% and 2.70%, respectively. Therefore, it can be concluded that the absence of S atoms leads to the formation of S vacancies that are positive charged (electron deficient), which has the potential to facilitate the capture of metal atoms (electron donors). Moreover, it is found that the inward relaxation of the V_{S2} is greater than that of the V_S as the V_{S2}-Mo_{NA} and the V_{S2}-S_{NA} distances are shortened by 5.47% and 3.53% respectively (Table 1). This means that after relaxation, distance between the Mo atoms and the S vacancy become shorter.

Therefore, the missing of S atoms leads to the formation of S vacancies that are positive charged (electron deficient), which would facilitate the capture of metal atoms (electron donors). Moreover, some researches have reported the adsorption of metals, such as Mn atom, Fe atom and Au cluster, on the Vs type of defects in MoS_2 nanosheet [44, 45], which shows the potential of Vs position in capturing metal atoms. Most of the trace Fe and Mn species were in dust form of flue gas at coal fired power plant that can be removed by existing air pollution control devices (APCDs) such as electrostatic

precipitator (ESP), fabric filters (FF). Therefore, most of the effective surface of the MoS_2 with Vs defect is active for capture airborne Hg^0.

3.1.2 ab initio mapping of MoS_2 surface

Theoretically, a more negative adsorption energy (E_{ads}) indicates a more favourable interaction between adsorbent and the adsorbate [46]. All potential adsorption sites on the defect-free and defective MoS_2 nanosheets were evaluated and numbered in the order of magnitude of the adsorption energy as shown in **Figure 1**.

Based on ab initial calculations, it is clear that on the defect-free MoS_2 nanosheets, the strongest adsorption site is Position 18, which is the position on top of a Mo atom. This suggests that the adsorption of Hg^0 on the MoS_2 nanosheets is affected by S and Mo atoms in a synergistic manner.

For the defective structure with one absent Mo atom (V_{Mo}), the site with the second highest absolute adsorption energy (Position 21) is also found to be on top of a Mo atom. However, for this V_{Mo} structure, the strongest adsorption site is on top of the hollow space of the sulphur plane (Position 2). This is mainly due to the repulsive force against Hg^0 atom from the negatively charged V_{Mo}. With the absence of Mo atom, the adsorption energy of V_{Mo} is significantly lower than that of the other positions on the defective surfaces and the defect-free surface. This further indicates that Mo atoms affect the adsorption of Hg^0 on MoS_2 nanosheets.

Based on ab initio calculations, it is clear that Hg^0 adsorption occurred on the MoS_2 nanosheets with V_{S2} and V_S showed similar behaviours. For both cases, the adsorption site with the second largest absolute adsorption energy, Position 2 for V_S and Position 11 for V_{S2}, are on top of Mo atoms, with an adsorption energy of approximately 1.12 eV. Furthermore, for the adsorption of mercury atoms on defective MoS_2 nanosheets, i.e., V_{S2} and V_S, the most stable adsorption sites are the ones right above the original position

of the absent S atoms, i.e., on top of the S vacancies. It is found that for the structure with only one absent sulphur atom, the absolute adsorption energy is slightly greater than that of the structure with two absent sulphur atoms, which indicates stronger attraction to Hg^0 on the V_S than on the V_{S2}. These results suggest that the S vacancies have major influence on the adsorption of Hg^0, while the absence of an additional S atom in the V_{S2} has less influence on the adsorption process.

In order to quantify the interactions between Hg^0 and the different types of vacancies on a MoS_2 surface, p-band centre analysis was carried out following a similar method as the d-band centre analysis for transition metals [37]. Compared with PDOS or DOS of each element in MoS_2 as shown in

Figure 2, it can be found that both the s and p orbitals of S atoms and s and p orbitals of Mo atoms have some noticeable influence on the adsorption of Hg^0. Moreover, p-band centre analysis was also carried out in this study to show the bonding strength of mercury adsorption on different types of defects in MoS_2 surface. The variation in binding energy (Equation (1)) is determined by the $|\varepsilon_p - \varepsilon_s|$, which is plotted in **Figure 3** (a). The closer of p band center to the Fermi level indicates the greater interaction between s orbital of the Hg^0 atom with p orbitals of the defective MoS_2 surface. Based on p-band center analysis, it is found that adsorption energy is in the order of $V_S > V_{S2} > V_{Mo}$. Therefore, it can be concluded that V_S is the strongest sites for Hg^0 adsorption.

Generally, defects with different formation energy can affect the physical and chemical properties of the MoS_2 monolayers, which could subsequently influence adsorption[47]. To further reveal the adsorption of Hg^0 on different defects in the MoS_2 surfaces, relationship between formation energy (E_V) of the defects and adsorption energy was studied using Equations (2) and (3), the results of which are shown in **Figure 3** (b). The smaller positive E_v value suggests that the formation of the vacancy is endothermic and

easier to form. As shown in Figure 3 (b), the V_S had the lowest formation energy. This is consistent with findings of other researchers that the V_S is frequently observed in MoS_2 surfaces [48]. The formation energy of V_{S2} was higher than that of V_s, which is consistent with reported finding that randomly distributed V_s is more frequently observed than V_{s2} [48]. The formation energy of V_{Mo} is even higher than that of V_{S2}. These results further indicate that the Vs is the most stable configuration for Hg^0 adsorption and the Vs is the prevailing defect in MoS_2 nanosheets.

3.2 Experimental Study

3.2.1 Preparation of defective MoS_2 nanosheets

In this study, a novel approach based on FactSage™ (version 6.3) with phase diagram module was developed to determine conditions for sample preparation, such as concentration of precursors and temperature for preparation, which is to avoid problems associated with traditional trial-and-error approach in sample preparation. **Figure 4** (a) illustrates preparation conditions for the formation of MoS_2 sample via sulphur-chemical vapour reaction (S-CVR) process. This triangle phase diagram indicated that the calcined material (mainly consists of MoO_3) reacts with H_2S and H_2 gas mixture with different mole fractions at 400 °C and results in the formation of various stable phases, such as MoS_2, MoO_2, Mo_4O_{11}, Mo_8O_{23} and Mo_9O_{26}. It is clear that to prepare MoS_2 as the main component of the adsorbent, the calcined adsorbent should be sulphided at 400 °C in the atmosphere of H_2S (10 vol.%) /H_2 (90 vol.%). It can be concluded that the graphene-like MoS_2-containing adsorbent (with a surface area around 204 m^2/g) was prepared on the mesoporous γ-Al_2O_3 (with 211 m^2/g surface area) in a well-controlled manner. This novel method developed in this study can also be used in the controlled synthesis of other materials for environmental applications.

3.2.2 Characterization of Defective MoS_2 Nanosheets

The samples prepared were then characterized by using a number of techniques. The well-dispersed chemical species and the chemical state on the surface of samples were further investigated by using XPS analysis[49, 50].The stable phases of the Mo 3d XPS spectra are as shown in **Figure 4**(b). According to the XPS database (version 4.1) of NIST Chemistry WebBook [51], the peaks with binding energy (BE) of approximately 232.8 eV, 228.8 eV, 162.6 eV are assigned to Mo^{4+} 3d3/2, Mo^{4+} 3d5/2 and S 2p, respectively. Therefore, it is proved that MoS_2 was successfully prepared in this study. This also confirmed that it is feasible to use FactSage™ to guide the preparation of samples with desired phase of the active components.

The S-Mo-S layered structure was then characterized by Raman spectroscopy. As shown in **Figure 4**(c), the Raman spectra show two strong peaks at the in-plane E^1_{2g} and the out-of-plane A_{1g} vibration, which are the typical peaks of MoS_2 nanosheets. Normally the peak positions of E^1_{2g} and A_{1g} bands are the strong indicator of the number of layers [52]. **Figure 4** (c) shows the peak positions of E^1_{2g} and A_{1g} bands, which are 378.72cm^{-1} and 404.11cm^{-1}, respectively. The peak position of A_{1g} bands (out-of-plane vibration, see the schematic diagram inside the **Figure 4**(c)) is consistent with that of 1-3 layers. However, the frequency of E^1_{2g} bands (i.e., in-plane vibration) decreased when compared with what was reported for pristine MoS_2 (384 cm^{-1})[52]. The significant shift of E^1_{2g} mode and almost unchanged A_{1g} mode correspond to sulphur vacancies in MoS_2 [47].

Moreover, XRD analysis was conducted to show structure of the MoS_2 on γ-Al_2O_3 support. Only three major peaks at around 37, 47 and 67 degrees can be identified as shown in **Figure 4**(d) (ii), which are the characteristic peaks of γ-Al_2O_3 crystal (as shown in **Figure 4**(d)(i)). There are no visible diffraction peaks of Mo species, which is an indication that MoS_2 is well-dispersed on the support and forms monolayers (nanosheets) [53].

Morphology of the adsorbent prepared was further characterized using a HRTEM as shown in **Figure 4**(e). It can be seen that the regular interplanar spacing is 0.27 nm. This is the characteristic pattern of (001) planes of the hexagonal MoS_2 crystal structure. Based on this observation, the schematic structure of the 2D-TMD MoS_2 nanosheets was proposed and illustrated inside the **Figure 4**(e). The HRTEM result is consistent with the other researchers' recent findings that the un-supported MoS_2 sample is defect-rich ultra-thin MoS_2 nanosheets [48]. In addition, there are many dislocations and distortions that can be observed in **Figure 4**(e), which also suggest that this type of MoS_2 nanosheets contains defects [48].

Moreover, NH_3 was selected as the probe molecule for the in-situ DRIFTS to characterize acidity of active centres (**Figure 4**(f)), which is to show the surface property and therefore to understand properties of the defect-rich MoS_2 nanosheet **[52]**. The peaks at around 1230, 1450, 1630, 1670, 2800, 3000 and 3200 cm^{-1} remained after NH_3 adsorption and N_2 purging. Normally, peaks at 1230 cm^{-1} and 1630 cm^{-1} are the characteristic pattern of the absorbed NH_3 molecules on Lewis acid sites, whilst peaks at 1450 cm^{-1} and 1670 cm^{-1} are the coordinated NH_4^+ species on Brønsted acid sites [54]. The peaks at 2800, 3000 and 3200 cm^{-1} in the stretching region are associated with the NH_4^+ bands. It is obvious that the intensity of Brønsted acid sites of the MoS_2 material was higher than that of Lewis acid sites.

Surface acidity was further investigated by using NH_3-TPD. The NH_3 desorption peaks at low temperatures are attributed to the Brønsted acid sites, whereas those peaks at high temperatures are assigned to Lewis acid sites [27]. As shown in **Figure 4**(f), the strong desorption peaks are observed at temperature below 250 °C, which further confirms that surface of the MoS_2 nanosheets is dominated by Brønsted acid sites. The amount of NH_3 adsorbed at Brønsted acid sites can be associated with the existence of coordinative unsaturated sites (CUS) on surface of the defect-rich MoS_2 nanosheets [55]. The

formation of Vs on the MoS_2 nanosheets might result in high Hg^0 adsorption efficiency as previously predicted by computational results.

3.2.3 Evaluation of Defective MoS_2 Nanosheets for Hg^0 Adsorption

Mercury adsorption capability of the defective MoS_2 nanosheets was then evaluated by using the IDSS experimental method. **Figure 5**(a) shows that the adsorbent demonstrated excellent performance in the adsorption of Hg^0 at temperatures below 150°C. The steady-state analysis (as shown in **Figure 5**(b)) further demonstrates that the Vs-rich MoS_2 nanosheets show excellent performance in Hg^0 adsorption with almost 100% removal efficiency.

It is found that the adsorbed Hg^0 could then be desorbed when temperature was raised to above 200°C with the calculated ratio of desorption over adsorption exceeding 99.4%. This suggests that the MoS_2 nanosheet containing materials can be regenerated easily at high temperature. This property makes MoS_2 nanosheet containing material a better adsorbent both technically and economically, as compared with activated carbon injection technology. In addition, this V_s-rich MoS_2 nanosheets demonstrates the potential to recover the captured Hg^0 efficiently as a resource without having any impacts on the saleability of fly ash as a product.

3.3 Hg^0 adsorption mechanism

Mechanism of the adsorption of Hg^0 on the Vs-rich MoS_2 surface was further studied by the charge density difference analysis, PDOS analysis, and adsorption pathways and energy profiles predictions.

Plots of the charge-density difference for Hg^0 adsorption on the Vs, Vs_2 and V_{Mo} are shown in **Figure 6**. The blue area covered the entire S vacancy, which means charge density increased in this area.

Atomic charges for Vs in MoS_2 monolayer and corresponding Hg^0-MoS_2 nanosheets were calculated by using Mulliken method. Table 2 shows the electron transfer through Hg^0-

MoS_2 (001) interactions with Vs, Vs_2 and V_{Mo}. The charge transfer was based on the difference between the original state and the adsorption state. A positive value means the atom obtains electrons after adsorption, while a negative value indicates the atom loses electrons after adsorption.

Results of Mulliken charge analysis (as illustrated in Table 2) showed that the electrons transferred a charge of 0.02eV from the Hg atom (6s) to S atom (3p) through the sulphur vacancy (Vs), and the Mo atom (4p) also transfers a charge of 0.01eV to the S surface, which enhanced the electronegativity of the vacancy (shown in blue area). There are charge-charge interactions between Hg^0 and the Vs, which indicates that Hg^0 atoms are chemically adsorbed on the surface. The order of the magnitude of adsorption energy at Vs (as shown in Figure 1) also corresponds to chemical interactions between the surface and the mercury atoms adsorbed [56]. The distance from the mercury atom to the Vs is short as shown in Figure 7. Since the distance from the Hg^0 atom to the NA S atoms is shorter than the sum of the covalent radii by 40%[57], it is confirmed again that the Hg atom is chemically adsorbed on the Vs.

To further understand the adsorption of Hg^0 atoms on MoS_2 (Vs) nanosheets, the density of state (DOS) of the surface atoms was studied in depth. The partial density of states (PDOS) of Hg, Mo and S atoms were calculated and are shown in

Figure 2. The PDOS peaks of d, s and p orbitals of an isolated Hg^0 atom are close to -3.1, 0 and 5.7eV, respectively. After adsorption, all the PDOS peaks of the Hg atom shifted left with the state of s and p orbitals significantly decreased in energy level. This suggested that there are strong interactions between Hg^0 and MoS_2 (Vs-rich) nanosheets. As shown in

Figure 2 (a), no noticeable shift in d states of the Mo atom was observed, which suggests that 4d orbitals of Mo atoms does not have noticeable influence on the adsorption of Hg^0. Among these notable features of the PDOS changes, it is worth mentioning that the

peak at -4 eV of PDOS(d) of Hg atoms overlaps with the major peak in the PDOS(s) of Mo atoms and PDOS(s) of sulphur atoms. This indicates the repulsive force between Hg atoms and MoS_2 nanosheets may be from the filled s orbitals of S, d orbitals of Hg and unfilled s orbitals of Mo. Compared with the PDOS of p states of Mo and S atoms before and after adsorption, both strongly overlapped with the s and p states of Hg atoms at approximately -0.9 eV and 2.3 eV (the value of DOS, 0.1/ eV), respectively. All of these suggest that Hg^0 atoms interact strongly with the MoS_2 surface, and the p states of both Mo and S atoms play important roles in the adsorption of mercury. This is also the reason why the p-band centre analysis was developed for potential adsorption sites evaluation. Figure 8 illustrates the adsorption pathways and energy profiles of a Hg^0 atom adsorbed on the Vs in MoS_2 (001) surface. The result represents the minimum energy path for the diffusion of an Hg^0 atom between Position 9 and Position 1 as shown in Figure 1.

Based on the fully optimized adsorption geometry of the Vs of MoS_2 (001) nanosheet (monolayer) (as shown in Figure 1(a)), nine stable adsorption configurations were identified. As discussed, Position 1 corresponds to a Hg atom adsorbed on top of the S vacancy, which is the most stable adsorption site. Position 9 represents the adsorption of a Hg atom on top of an S atom, which is the second NA S atom to the vacancy with the minimum adsorption energy. The minimum energy paths for the diffusion of an Hg atom between different adsorption configurations using NEB calculations were further investigated and are shown in Figure 8.

The NA Mo atoms around the S vacancy make the Hg adsorption configuration unstable, which is caused by the interactions between the Hg cations and the Mo cations. Furthermore, the positive charge (electron deficient) of Vs attracts the Hg atom to the centre of the vacancy. As discussed previously, the inward relaxation makes the surface of MoS_2 become a sunken cave. As shown in Figure 8, the pathway between Position 9 and Position 1, from high energy level to low energy level, has no energy barrier for the

adsorption to occur. Based on the adsorption pathways and energy profiles predictions, the adsorption could be classified as non-activated chemisorption, which is introduced by surface defects (V_S), which exhibit high adsorption probability[58]. The IDSS experimental observation indicated that the Vs containing MoS_2 nanosheets are able to adsorb Hg^0 at lower temperatures, which is consistent with ab initio calculation computational investigation. It can therefore be concluded that the adsorption of Hg^0 atom around the Vs is non-activated chemisorption.

4. Conclusions

In this study, the ab initio calculation showed that S vacancies (Vs) in the MoS_2 nanosheets exhibited outstanding potential in Hg^0 adsorption among different structural defects. The MoS_2 material was successfully prepared in a controlled manner under conditions that were determined via phase diagrams that are generated using Factsage. Results of characterisation work confirmed that the MoS_2 material consists of nanosheets and is of graphene-like layered structure with abundant defects. Moreover, the existence of coordinative unsaturated sites (CUS) on the surface of the defect-rich MoS2 nanosheets was confirmed by the NH_3-TPD and in-situ DRIFTS by using NH_3 as a probe molecule. Moreover, the experimental results confirmed that this Vs-rich nanosheets showed excellent Hg^0 adsorption. The adsorption of Hg^0 on Vs was found to be non-activated chemisorption.

Acknowledgements

National Key Research and Development Projects (2017YFB0603202 and 2017YFC0210400), National Natural Science Foundation of China (51836006, 51706114), and Ningbo Natural Science Foundation (2017A610060) are acknowledged for partially sponsoring this research. Authors 1 and 2 contributed equally to this work.

References

[1] F.D. Simone, C.N. Gencarelli, I.M. Hedgecock, N. Pirrone, A Modeling Comparison of Mercury Deposition from Current Anthropogenic Mercury Emission Inventories, Environmental Science & Technology, 50 (2016) 5154-5162.
[2] Y. Liao, D. Chen, S. Zou, S. Xiong, X. Xiao, H. Dang, T. Chen, S. Yang, Recyclable Naturally Derived Magnetic Pyrrhotite for Elemental Mercury Recovery from Flue Gas, Environmental Science & Technology, 50 (2016) 10562-10569.
[3] Y. Ma, B. Mu, D. Yuan, H. Zhang, H. Xu, Design of MnO2/CeO2-MnO2 hierarchical binary oxides for elemental mercury removal from coal-fired flue gas, Journal of Hazardous Materials, 333 (2017) 186-193.
[4] Y. Gao, Z. Zhang, J. Wu, L. Duan, A. Umar, L. Sun, Z. Guo, Q. Wang, A Critical Review on the Heterogeneous Catalytic Oxidation of Elemental Mercury in Flue Gases, Environmental Science & Technology, 47 (2013) 10813-10823.
[5] D.-H. Lim, J. Wilcox, Heterogeneous Mercury Oxidation on Au(111) from First Principles, Environmental Science & Technology, 47 (2013) 8515-8522.
[6] J. Yang, M. Zhang, H. Li, W. Qu, Y. Zhao, J. Zhang, Simultaneous NO Reduction and Hg0 Oxidation over La0.8Ce0.2MnO3 Perovskite Catalysts at Low Temperature, Industrial and Engineering Chemistry Research, 57 (2018) 9374-9385.
[7] J. Yang, Y. Zhao, S. Liang, S. Zhang, S. Ma, H. Li, J. Zhang, C. Zheng, Magnetic iron–manganese binary oxide supported on carbon nanofiber (Fe3−xMnxO4/CNF) for efficient removal of Hg0 from coal combustion flue gas, Chemical Engineering Journal, 334 (2018) 216-224.
[8] UNEP, Global Mercury Assessment 2013: Sources, emissions, releases, and environmental transport [Online] available from <http://www.unep.org> (accessed December 20, 2017), in, 2013.
[9] H. Cheng, Y. Hu, Mercury in Municipal Solid Waste in China and Its Control: A Review, Environmental Science & Technology, 46 (2012) 593-605.
[10] P.T. Bolger, D.C. Szlag, An Electrochemical System for Removing and Recovering Elemental Mercury from a Gas Stream, Environmental Science & Technology, 36 (2002) 4430-4435.
[11] A.M. Kunkel, J.J. Seibert, L.J. Elliott, R. Kelley, L.E. Katz, G.A. Pope, Remediation of Elemental Mercury Using in Situ Thermal Desorption (ISTD), Environmental Science & Technology, 40 (2006) 2384-2389.
[12] S.M. Wilhelm, Estimate of Mercury Emissions to the Atmosphere from Petroleum, Environmental Science & Technology, 35 (2001) 4704-4710.
[13] Y. Zhao, R. Hao, Q. Guo, A novel pre-oxidation method for elemental mercury removal utilizing a complex vaporized absorbent, Journal of Hazardous Materials, 280 (2014) 118-126.
[14] C. Rungnim, V. Promarak, S. Hannongbua, N. Kungwan, S. Namuangruk, Complete reaction mechanisms of mercury oxidation on halogenated activated carbon, Journal of Hazardous Materials, 310 (2016) 253-260.
[15] S. Aboud, E. Sasmaz, J. Wilcox, Mercury adsorption on PdAu, PdAg and PdCu alloys, Main Group Chemistry, 7 (2008) 205-215.
[16] H. Zhao, G. Yang, X. Gao, C.H. Pang, S.W. Kingman, T. Wu, Hg0 Capture over CoMoS/γ-Al2O3 with MoS2 Nanosheets at Low Temperatures, Environmental Science & Technology, 50 (2016) 1056-1064.
[17] T.M. Bisson, Z. Xu, Potential Hazards of Brominated Carbon Sorbents for Mercury Emission Control, Environmental Science & Technology, 49 (2015) 2496-2502.
[18] H. Li, L. Zhu, J. Wang, L. Li, K. Shih, Development of nano-sulfide sorbent for efficient removal of elemental mercury from coal combustion fuel gas, Environmental Science and Technology, 50 (2016) 9551-9557.
[19] H. Li, W. Zhu, J. Yang, M. Zhang, J. Zhao, W. Qu, Sulfur abundant S/FeS2 for efficient removal of mercury from coal-fired power plants, Fuel, 232 (2018) 476-484.
[20] J. Yang, Y. Zhao, X. Guo, H. Li, J. Zhang, C. Zheng, Removal of elemental mercury from flue gas by recyclable CuCl2 modified magnetospheres from fly ash. Part 4. Performance of sorbent injection in an entrained flow reactor system, Fuel, 220 (2018) 403-411.
[21] Q.H. Wang, K. Kalantar-Zadeh, A. Kis, J.N. Coleman, M.S. Strano, Electronics and optoelectronics of two-dimensional transition metal dichalcogenides, Nature nanotechnology, 7 (2012) 699.
[22] M. Chhowalla, H.S. Shin, G. Eda, L.-J. Li, K.P. Loh, H. Zhang, The chemistry of two-dimensional layered transition metal dichalcogenide nanosheets, Nat Chem, 5 (2013) 263-275.
[23] L. Yang, X. Zheng, M. Liu, S. Luo, Y. Luo, G. Li, Fast photoelectro-reduction of CrVI over MoS2@TiO2 nanotubes on Ti wire, Journal of Hazardous Materials, 329 (2017) 230-240.

[24] D. Song, Q. Li, X. Lu, Y. Li, Y. Li, Y. Wang, F. Gao, Ultra-thin bimetallic alloy nanowires with porous architecture/monolayer MoS2 nanosheet as a highly sensitive platform for the electrochemical assay of hazardous omethoate pollutant, Journal of Hazardous Materials, 357 (2018) 466-474.
[25] K. Zhou, R. Gao, X. Qian, Self-assembly of exfoliated molybdenum disulfide (MoS2) nanosheets and layered double hydroxide (LDH): Towards reducing fire hazards of epoxy, Journal of Hazardous Materials, 338 (2017) 343-355.
[26] L. Shi, W. Ding, S. Yang, Z. He, S. Liu, Rationally designed MoS2/protonated g-C3N4 nanosheet composites as photocatalysts with an excellent synergistic effect toward photocatalytic degradation of organic pollutants, Journal of Hazardous Materials, 347 (2018) 431-441.
[27] H. Zhao, G. Yang, X. Gao, C. Pang, S. Kingman, E. Lester, T. Wu, Hg0-temperature-programmed surface reaction and its application on the investigation of metal oxides for Hg0 capture, Fuel, 181 (2016) 1089-1094.
[28] H. Zhao, H. Fan, G. Yang, L. Lu, C. Zheng, X. Gao, T. Wu, Integrated Dynamic and Steady State Method and Its Application on the Screening of MoS2 Nanosheet-Containing Adsorbents for Hg0 Capture, Energy & Fuels, 32 (2018) 5338-5344.
[29] H. Zhao, X. Mu, G. Yang, M. George, P. Cao, B. Fanady, S. Rong, X. Gao, T. Wu, Graphene-like MoS2 containing adsorbents for Hg0 capture at coal-fired power plants, Applied Energy, 207 (2017) 254-264.
[30] H. Zhao, G. Yang, X. Mu, P. Cao, X. Gao, T. Wu, Hg0 Capture over MoS2 Nanosheets Containing Adsorbent: Effects of Temperature, Space Velocity, and Other Gas Species, Energy Procedia, 105 (2017) 4408-4413.
[31] H. Zhao, G. Yang, X. Mu, K. Shi, X. Gao, T. Wu, Recovery of Elemental Mercury from Coal-derived Flue Gas using a MoS2-based Material, Energy Procedia, 142 (2017) 3584-3589.
[32] H. Zhao, X. Luo, J. He, C. Peng, T. Wu, Recovery of elemental sulphur via selective catalytic reduction of SO2 over sulphided CoMo/γ-Al2O3 catalysts, Fuel, 147 (2015) 67-75.
[33] F. Ortmann, F. Bechstedt, W. G. Schmidt, Semiempirical van der Waals correction to the density functional description of solids and molecular structures, Physical Review B, 73 (2006) 205101.
[34] D. Vanderbilt, Soft self-consistent pseudopotentials in a generalized eigenvalue formalism, Physical Review B, 41 (1990) 7892-7895.
[35] D. Liu, X. Chen, D. Li, F. Wang, X. Luo, B. Yang, Simulation of MoS2 crystal structure and the experimental study of thermal decomposition, Journal of Molecular Structure, 980 (2010) 66-71.
[36] F.H.B. Lima, J. Zhang, M.H. Shao, K. Sasaki, M.B. Vukmirovic, E.A. Ticianelli, R.R. Adzic, Catalytic Activity−d-Band Center Correlation for the O2 Reduction Reaction on Platinum in Alkaline Solutions, The Journal of Physical Chemistry C, 111 (2007) 404-410.
[37] A. Vojvodic, J.K. Nørskov, F. Abild-Pedersen, Electronic Structure Effects in Transition Metal Surface Chemistry, Topics in Catalysis, 57 (2013) 25-32.
[38] Factsage, Phase Diagrams in, 2016.
[39] C. Zhou, X. Liu, C. Wu, Y. Wen, Y. Xue, R. Chen, Z. Zhang, B. Shan, H. Yin, W.G. Wang, NO oxidation catalysis on copper doped hexagonal phase LaCoO3: a combined experimental and theoretical study, Physical Chemistry Chemical Physics, 16 (2014) 5106-5112.
[40] C. Lee, H. Yan, L.E. Brus, T.F. Heinz, J. Hone, S. Ryu, Anomalous Lattice Vibrations of Single- and Few-Layer MoS2, ACS Nano, 4 (2010) 2695-2700.
[41] L. Zhong, R.C. Bruno, K. Ethan, L. Ruitao, R. Rahul, T. Humberto, A.P. Marcos, T. Mauricio, Defect engineering of two-dimensional transition metal dichalcogenides, 2D Materials, 3 (2016) 022002.
[42] X. Luo, B. Wang, Y. Zheng, First-principles study on energetics of intrinsic point defects in LaAlO3, Physical Review B, 80 (2009) 104115.
[43] T. Tanaka, K. Matsunaga, Y. Ikuhara, T. Yamamoto, First-principles study on structures and energetics of intrinsic vacancies in SrTiO3, Physical Review B, 68 (2003) 205213.
[44] W.T. Cong, Z. Tang, X.G. Zhao, J.H. Chu, Enhanced magnetic anisotropies of single transition-metal adatoms on a defective MoS2 monolayer, Sci Rep, 5 (2015) 9361.
[45] W. Ju, T. Li, X. Su, H. Li, X. Li, D. Ma, Au cluster adsorption on perfect and defective MoS2 monolayers: structural and electronic properties, Phys Chem Chem Phys, 19 (2017) 20735-20748.

[46] X.X. Xin Lu, Nanqin Wang, Qianer Zhang, A quantum chemical study of the NO/MgO chemisorption system: hybrid B3LYP calculations on NO/(MgO)n (n=4,6,8) model systems, Chemical Physics Letters, 300 (1999) 109-117.
[47] W.M. Parkin, A. Balan, L. Liang, P.M. Das, M. Lamparski, C.H. Naylor, J.A. Rodriguez-Manzo, A.T. Johnson, V. Meunier, M. Drndic, Raman Shifts in Electron-Irradiated Monolayer MoS2, ACS Nano, 10 (2016) 4134-4142.
[48] J. Xie, H. Zhang, S. Li, R. Wang, X. Sun, M. Zhou, J. Zhou, X.W. Lou, Y. Xie, Defect-Rich MoS2 Ultrathin Nanosheets with Additional Active Edge Sites for Enhanced Electrocatalytic Hydrogen Evolution, Advanced Materials, 25 (2013) 5807-5813.
[49] D. Jampaiah, S.J. Ippolito, Y.M. Sabri, J. Tardio, P.R. Selvakannan, A. Nafady, B.M. Reddy, S.K. Bhargava, Ceria–zirconia modified MnOx catalysts for gaseous elemental mercury oxidation and adsorption, Catalysis Science & Technology, 6 (2016) 1792-1803.
[50] S. Zhao, Y. Ma, Z. Qu, N. Yan, Z. Li, J. Xie, W. Chen, The performance of Ag doped V2O5–TiO2 catalyst on the catalytic oxidation of gaseous elemental mercury, Catalysis Science & Technology, 4 (2014) 4036-4044.
[51] U.S. NIST, NIST X-ray Photoelectron Spectroscopy Database (version 4.1) of NIST Chemistry WebBook in, 2015.
[52] J. Wilcox, E. Rupp, S.C. Ying, D.-H. Lim, A.S. Negreira, A. Kirchofer, F. Feng, K. Lee, Mercury adsorption and oxidation in coal combustion and gasification processes, International Journal of Coal Geology, 90-91 (2012) 4-20.
[53] M.-F. Luo, P. Fang, M. He, Y.-L. Xie, In situ XRD, Raman, and TPR studies of CuO/Al2O3 catalysts for CO oxidation, Journal of Molecular Catalysis A: Chemical, 239 (2005) 243-248.
[54] L. Chen, J. Li, M. Ge, DRIFT Study on Cerium−Tungsten/Titiania Catalyst for Selective Catalytic Reduction of NOx with NH3, Environmental Science & Technology, 44 (2010) 9590-9596.
[55] J.R. Anderson, M. Boudart, Catalysis - Science and Technology, Springer Berlin Heidelberg, Berlin, 1996.
[56] P.W. Atkins, Physical Chemistry, Oxford University Press, 2001.
[57] Y. Wang, B. Wang, R. Huang, B. Gao, F. Kong, Q. Zhang, First-principles study of transition-metal atoms adsorption on MoS2 monolayer, Physica E: Low-dimensional Systems and Nanostructures, 63 (2014) 276-282.
[58] K.D. Rendulic, A. Winkler, H.P. Steinrück, The role of surface defects in the adsorption and sesorption of hydrogen on Ni(111), Surface Science, 185 (1987) 469-478.

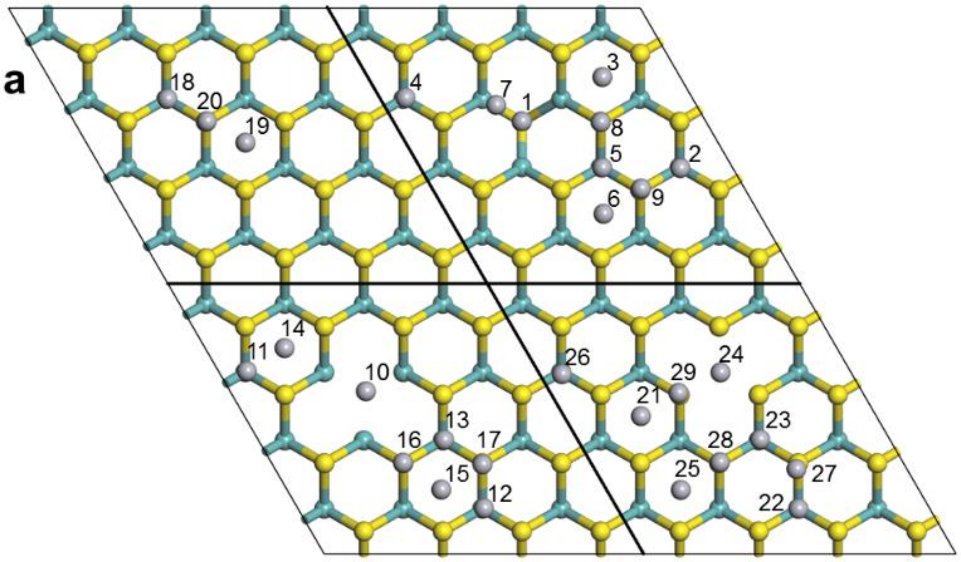

Figure 1 Potential Hg^0 adsorption sites in the MoS_2 surface and their corresponding adsorption energy. (a) Hg^0 adsorption sites and (b) Hg^0 adsorption energy

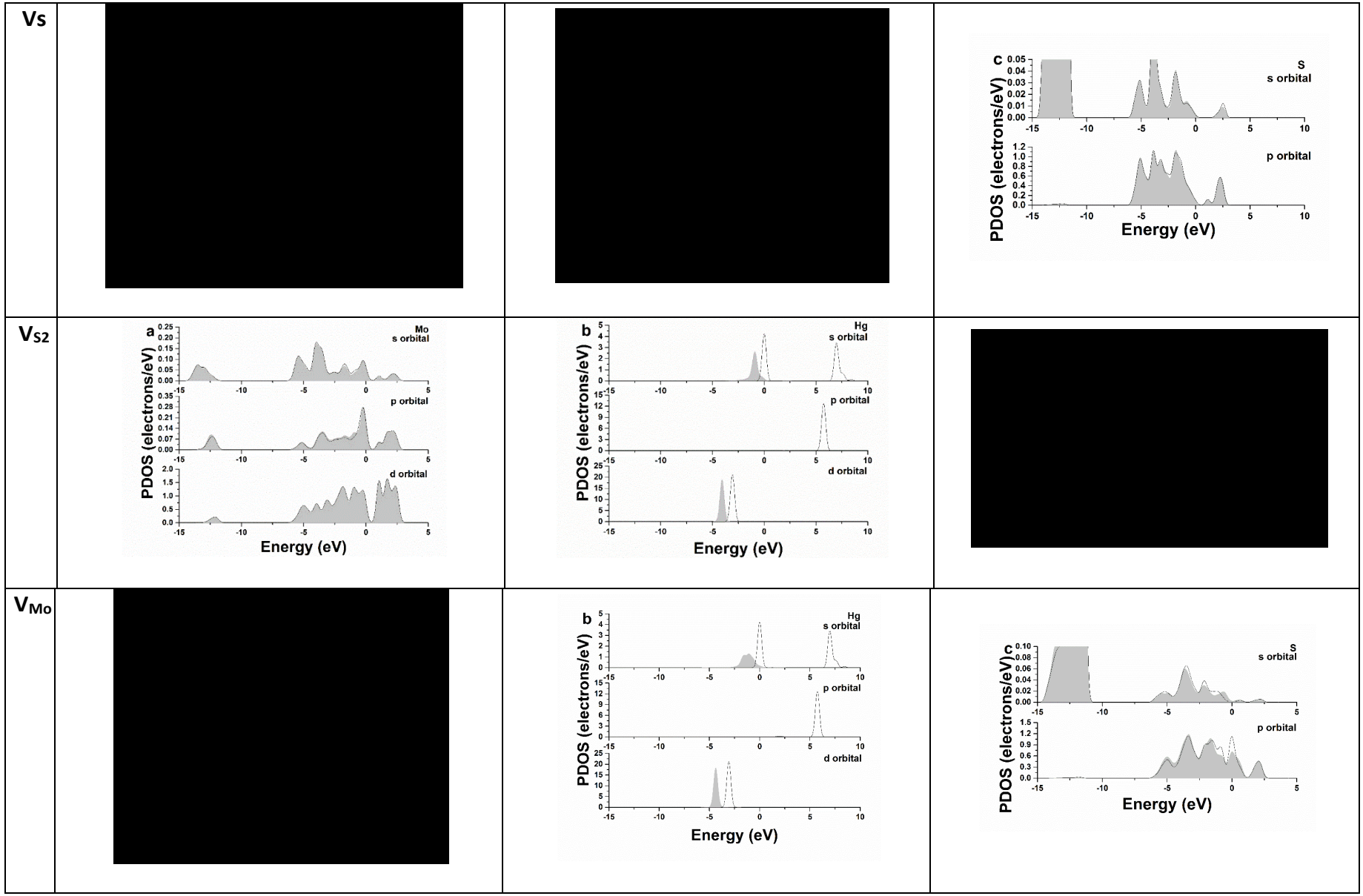

Figure 2 DOS analysis of a defective MoS_2 monolayer. (a) DOS of s orbital after adsorption, (b) DOS of p orbitals after adsorption, and, (c) DOS of d orbitals after adsorption. (Black line represents V_{S2}, the grey shadow represents V_S, red line represents V_{Mo}.

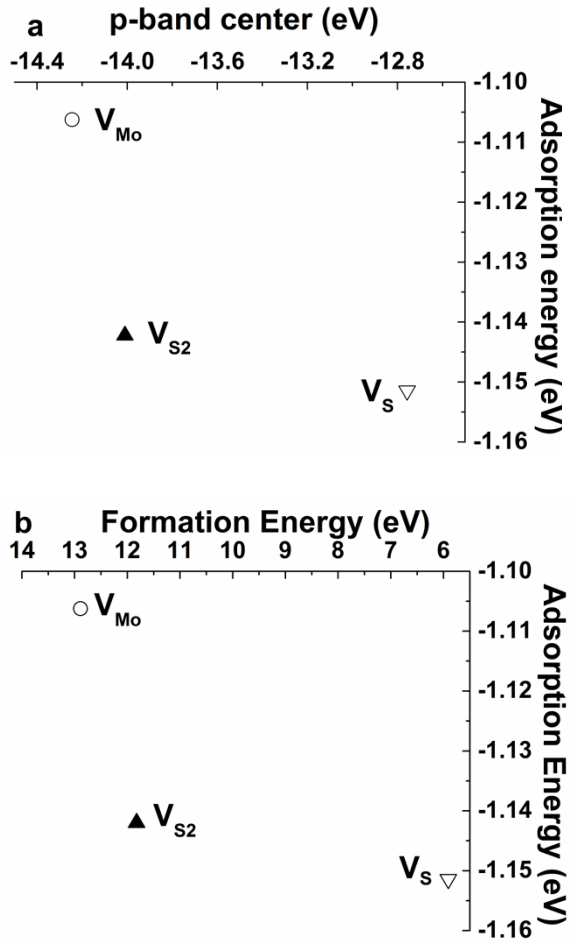

Figure 3 Different defects for Hg^0 capture. (a) p-band center analysis, and, (b) formation energy of defect for the most stable Hg^0 adsorption sites

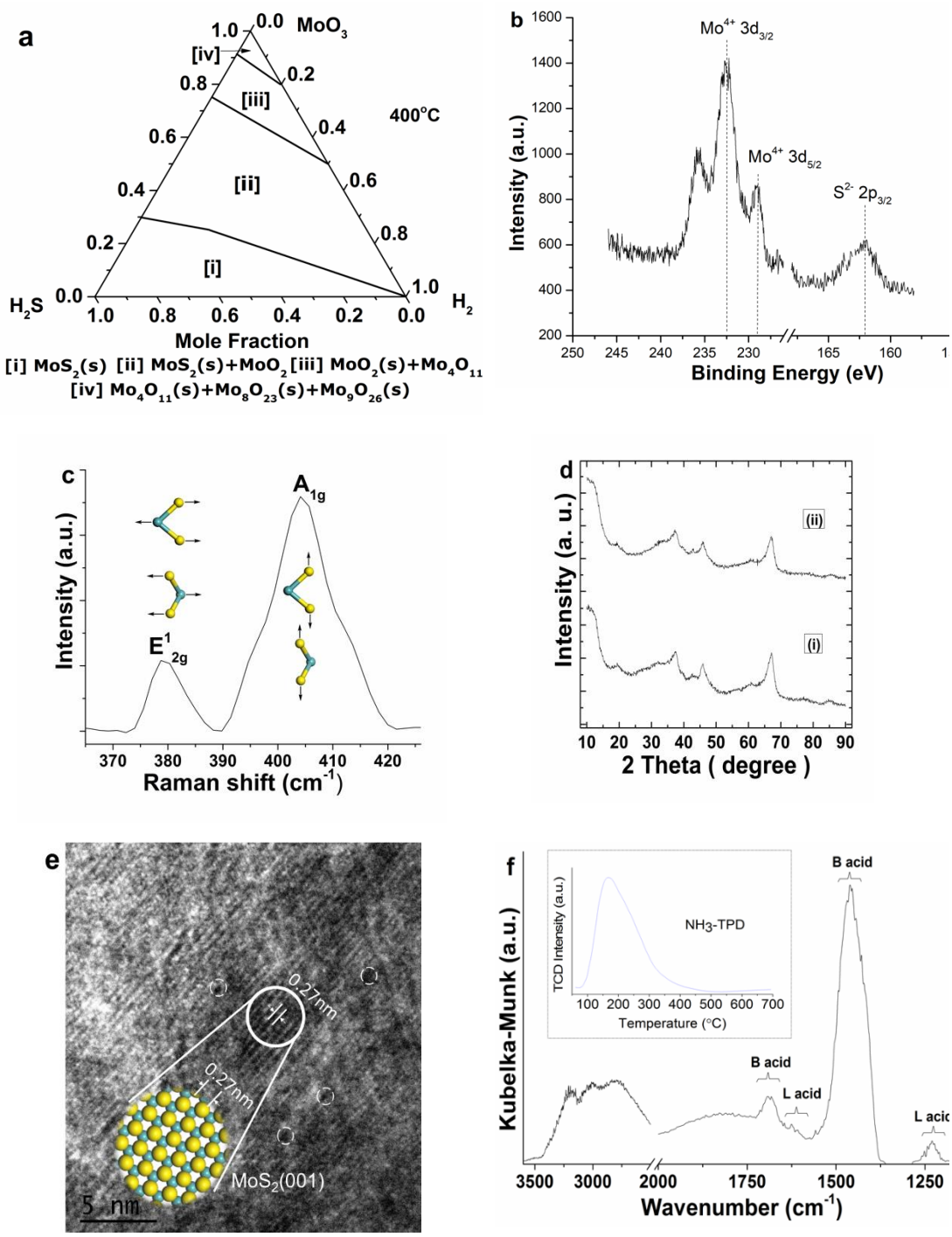

Figure 4 Preparation and characterization of MoS_2 nanosheets. (a) Phase diagram. (b) XPS spectra of Mo 3d and S 2p. (c) Raman spectra. (d) XRD analysis of γ-Al_2O_3 (i) and the MoS_2 containing adsorbent(ii). (e) HRTEM picture and schematic structure (enlarged image). (f) In-situ DRIFTS study and the NH_3-TPD profile (inserted figure).

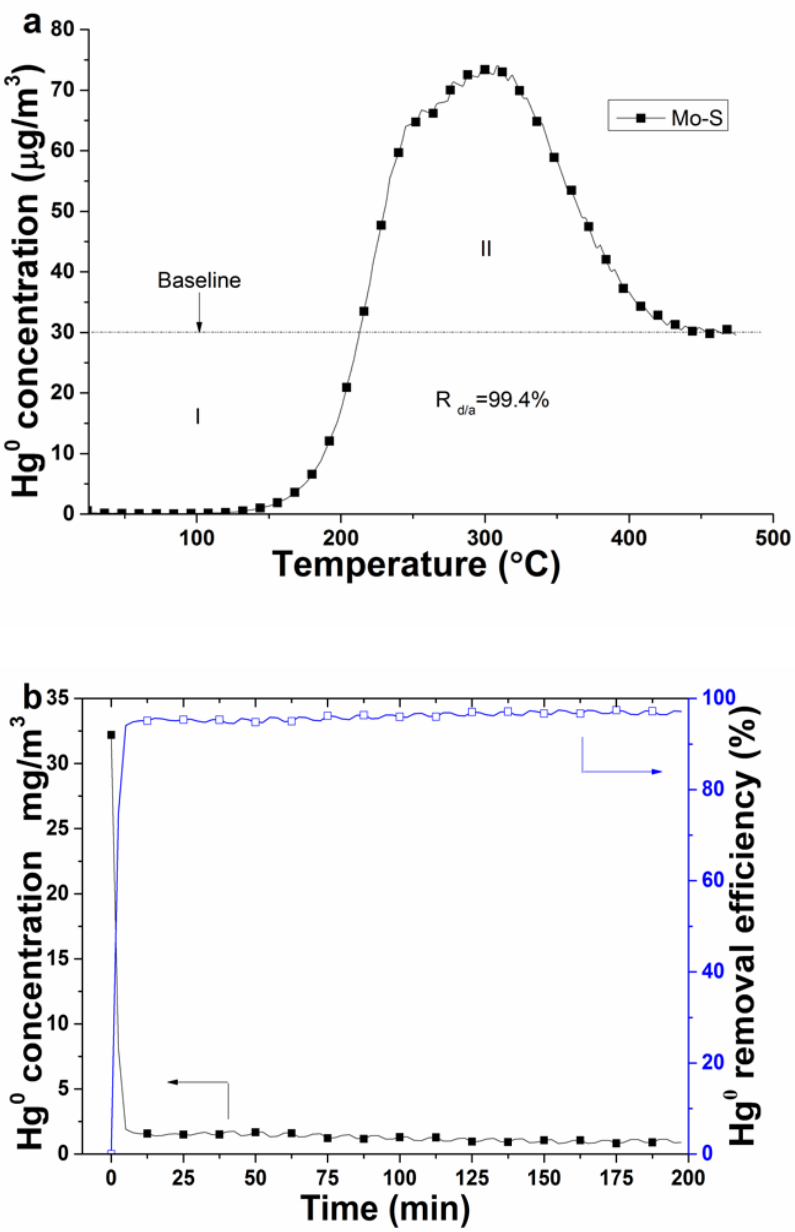

Figure 5 Hg^0 adsorption performance of Vs MoS_2 (001) containing adsorbent. (a) Dynamic transient and (b) steady-state experimental data

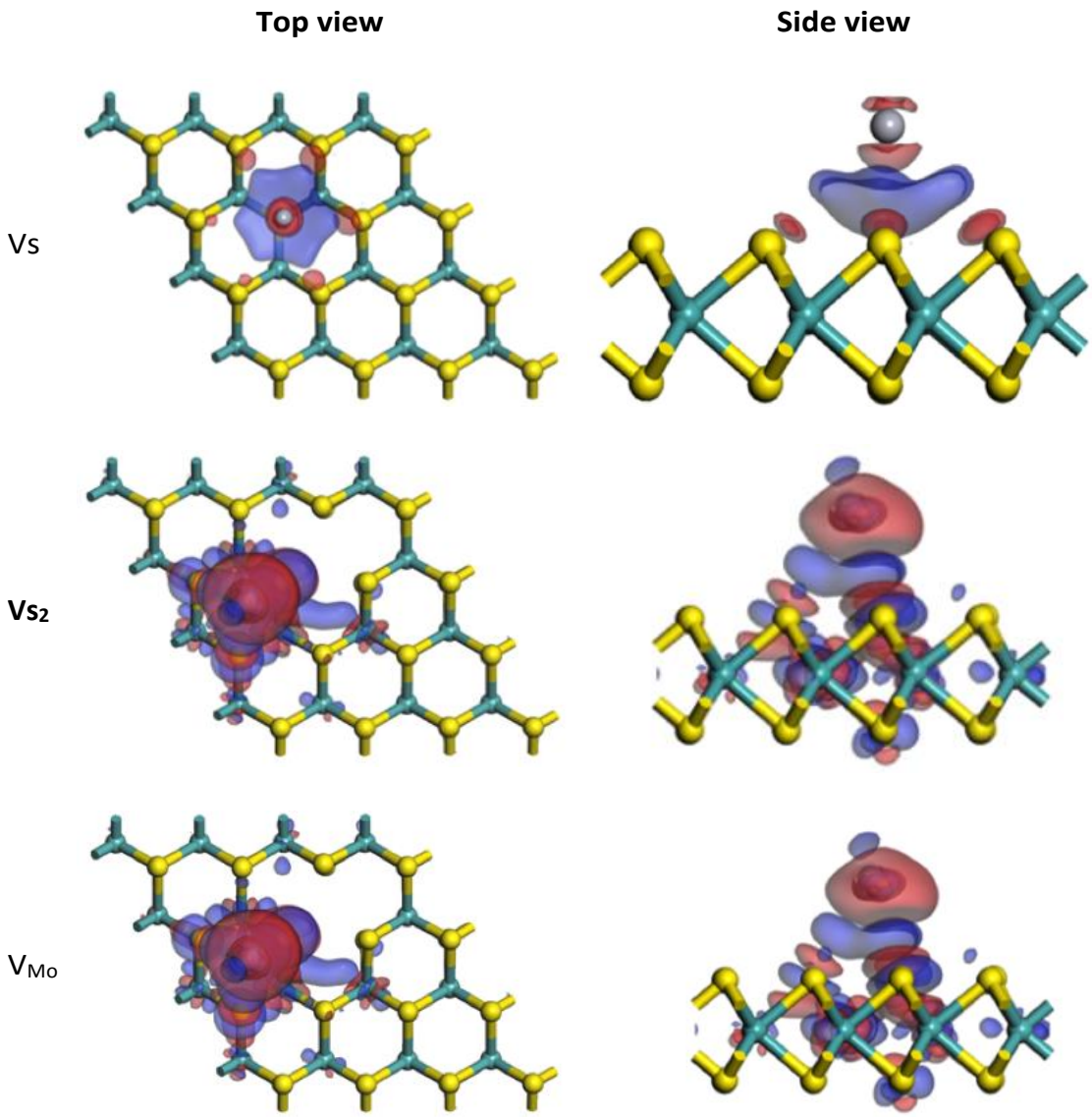

Figure 6 Charge density difference analysis of an Hg^0 atom adsorbed on different types of defects in MoS_2 (001) of the most stable configuration (iso-surface: 7.5×10-4 e/ $Å^3$).

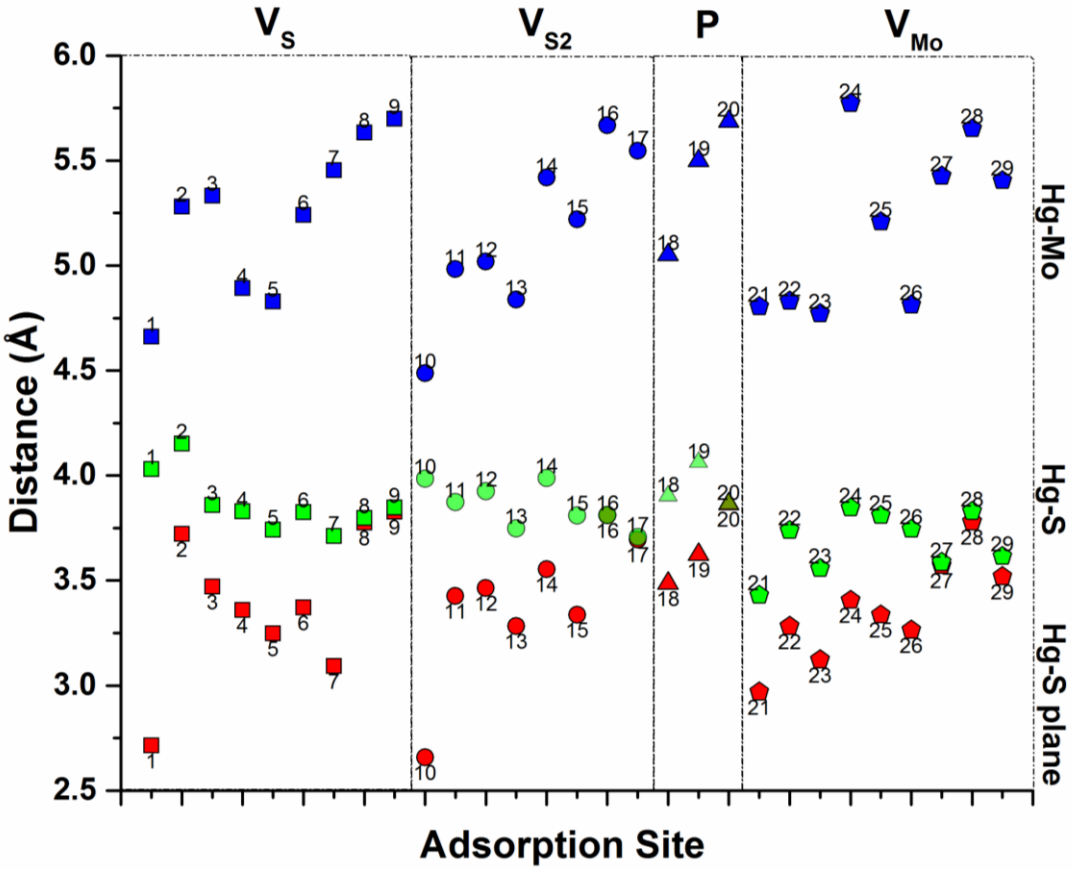

Figure 7 Hg^0 adsorption sites and the distances for different scenarios: Blue: distanceto its adjacent Mo atom; Green: distance to its adjacent S atom; Red: the distance to the upper layer of S atoms.

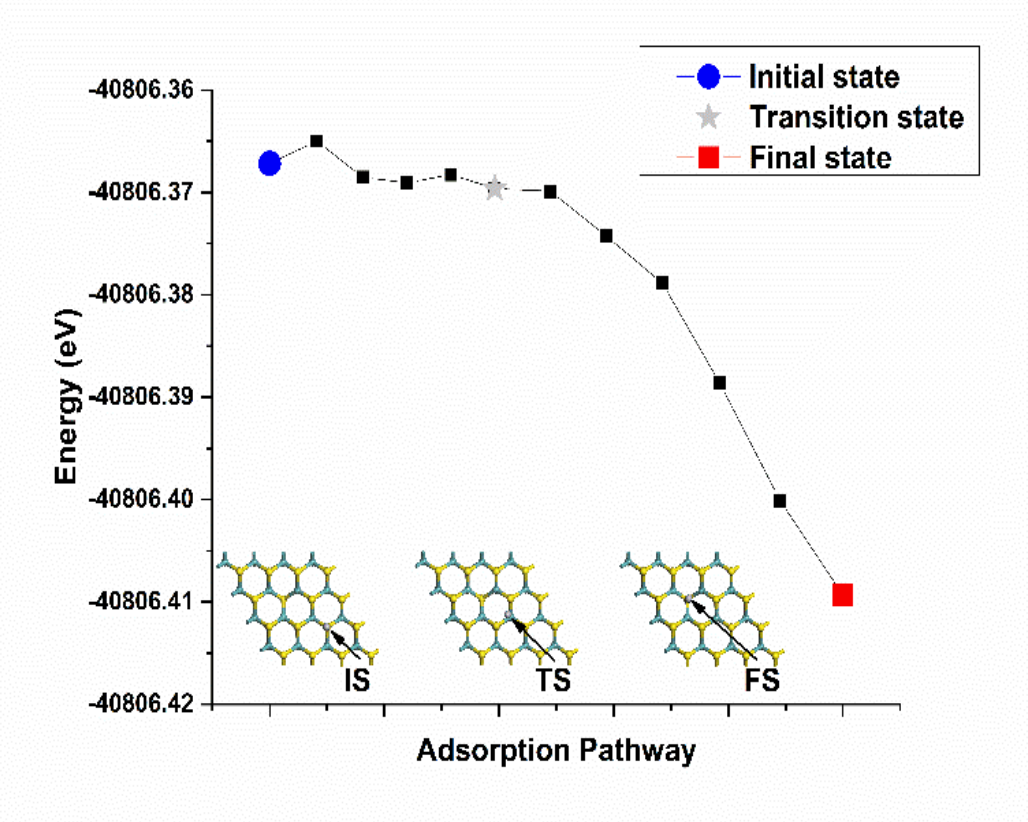

Figure 8 Adsorption pathways and energy profiles of the adsorption of an Hg^0 atom on the V_s MoS_2 (001) Surface.

Table 1 Distances from the vacancy to the NA atoms for MoS2 monolayer before and after geometry optimization.

Vacancy	Distance from vacancy to NA atoms(Å)			
	Along the S-Mo bond direction	δ%	Along the S-Mo bond direction	δ%
Vs	2.41(V- NA Mo)	-0.04%	3.097 (V- NA S)	-2.70%
Vs2	2.279(V- NA Mo)	-5.47%	3.071 (V- NA S)	-3.52%
Vmo	2.474(V- NA S)	2.61%	3.163 (V- NA Mo)	-0.63%
Perfect	2.411		3.183	

***** d(Mo-Mo)=d(S-S)= 3.183 Å

Table 2 Charge transfer of atoms for different defects determined by Mulliken Charge Analysis

Atom indexes	Vs			Atom indexes	V_{s2}			Atom indexes	V_{Mo}		
	Before	After	Electron Transfer		Before	After	Electron Transfer		Before	After	Electron Transfer
S(9)	-0.02	-0.01	-0.01	S(1)	-0.03	-0.02	-0.01	S(1)	-0.04	-0.03	-0.01
S(11)	-0.02	-0.01	-0.01	S(12)	-0.03	-0.02	-0.01	S(7)	-0.02	-0.01	-0.01
S(17)	-0.02	-0.01	-0.01	S(18)	-0.03	-0.02	-0.01	S(17)	-0.02	-0.01	-0.01
S(21)	-0.04	-0.03	-0.01	S(28)	-0.03	-0.02	-0.01	S(23)	-0.02	-0.03	0.01
S(26)	-0.02	-0.01	-0.01	S(29)	-0.03	-0.02	-0.01	S(24)	-0.02	-0.01	-0.01
S(28)	-0.02	-0.01	-0.01	Mo(2)	0.11	0.1	0.01	S(26)	-0.04	-0.03	-0.01
Mo(3)	0.05	0.06	-0.01	Mo(5)	0.01	-0.01	0.02	S(29)	-0.1	-0.09	-0.01
Mo(7)	0.04	0.02	0.02	Mo(10)	0.06	0.03	0.03	Mo(6)	0.1	0.07	0.03
Mo(13)	0.07	0.08	-0.01	Mo(14)	0.11	0.1	0.01	Mo(12)	0.07	0.08	-0.01
Mo(15)	0.04	0.02	0.02	Mo(15)	0.01	-0.01	0.02	Mo(14)	0.1	0.09	0.01
Hg	0	0.02	-0.02	Hg	0	0.02	-0.02	Hg	0	0.02	-0.02